The Astrophysical Journal Letters, 978:L2 (9pp), 2025 January 01 https://doi.org/10.3847/2041-8213/ad9a4f

A Flat-bottomed Buried Crater and Paleo-layered Structures Revealed at the Von Kármán Crater Using Lunar Penetrating Radar

Ling Zhang[1,2,5], Xindong Meng[1,5], Yuqi Qian[3], Yi Xu[1], Xiaoping Zhang[1], Zhipeng Liu[1], Jialong Lai[4], and Rui Gao[2]
[1] State Key Laboratory of Lunar and Planetary Sciences, Macau University of Science and Technology, Macau, People's Republic of China; yixu@must.edu.mo
[2] School of Earth Science and Engineering, Sun Yat-sen University, Guangzhou, People's Republic of China
[3] Department of Earth Sciences and Laboratory for Space Research, The University of Hong Kong, Hong Kong, People's Republic of China
[4] School of Science, Jiangxi University of Science and Technology, Ganzhou 341000, People's Republic of China
Received 2024 September 28; revised 2024 November 15; accepted 2024 November 27; published 2024 December 20

Abstract

Impact cratering is the most common geological process occurring on terrestrial planets. The morphologies of impact craters reflect not only the impact conditions but the target properties as well. They have been widely used as subsurface probes into regolith thickness and mechanical properties. A population of paleo-buried impact craters has been discovered by recent geophysical investigations of the Moon; however, their morphologies have never been constrained. The lunar penetrating radar onboard the Chang'e-4 rover has offered an unprecedented opportunity to study the morphology of those paleo-buried craters and reveal obscured depositing history. In this study, we have identified a flat-bottomed paleocrater (450 m in diameter; 11.5 m in depth) on an extraterrestrial world and reconstructed its morphology. This discovery reinforces how impacts would modify layered structures, providing additional evidence regarding subsurface interfaces between the paleoregolith layers and the final-stage lava layers, shedding light on similar processes on all planets.

Unified Astronomy Thesaurus concepts: The Moon (1692); Radar astronomy (1329); Lunar craters (949); Lunar regolith (2315); Lunar impacts (958)

1. Introduction

The impact process is the dominant exogenic geological process altering the surface of an airless planet, by fracturing, melting, and excavating the target and creating impact craters (H. J. Melosh 1989). The morphologies of impact craters vary with different impact conditions (impact velocity, impact angle, and impactor composition) and target properties, forming simple, transitional, and complex impact craters to even impact basins (G. R. Osinski et al. 2023). It has been well-recognized that layered impact targets are common in nearly all planets in the solar system (L. E. Senft & S. T. Stewart 2007) such as Earth (A. M. Stickle & P. H. Schultz 2013), the Moon (W. L. Quaide & V. R. Oberbeck 1968) and Mars (L. E. Senft & S. T. Stewart 2008). The formation of small impact craters (<∼500 m) is even more sensitive to shallow subsurface structures (W. L. Quaide & V. R. Oberbeck 1968; N. C. Prieur et al. 2018), generating normal, central-mound, flat-bottomed, and concentric craters. Therefore, the morphology of small craters has been widely used to constrain the subsurface properties of a planetary surface, especially the Moon (B. B. Wilcox et al. 2005; G. D. Bart et al. 2011; Y. Qian et al. 2021).

So far, the morphology of all lunar impact craters studied is according to the surface imagery data, e.g., the Narrow Angle Camera (NAC) images from the Lunar Reconnaissance Orbiter Camera (LROC), which provide key information for the top regolith (W. L. Quaide & V. R. Oberbeck 1968). However, a large population of buried impact craters has been recently identified on the Moon based on newly obtained geophysical data. Their morphologies have never been discussed, which may help to reveal the properties of paleoregolith and basalt layers and construct the complete depositing history. GRAIL gravity data have shown evidence of more than 100 quasi-circular mass anomalies (26–300 km in diameter) on the lunar nearside, which have been interpreted to be impact craters but buried by mare basalts (A. J. Evans et al. 2016). No small, buried impact craters have been found due to the resolution limitation of gravity data. lunar penetrating radar (LPR) is one of the key scientific payloads onboard the Chang'e-4 lunar rover, Yutu-2. It operates at two frequency channels (60 and 500 MHz) with vertical resolutions of 10 and 0.3 m, and detection depths of 500 and 50 m, respectively (C. Li et al. 2019). It offers another unique opportunity to recognize small craters that are more indicative of subsurface structures.

On 2019 January 3, the Chang'e-4 lunar probe successfully landed in the South Pole–Aitken Basin (SPA) (Figure 1(a)), achieving the first-ever soft landing on the far side of the Moon (W. Wu et al. 2019). The landing site was within the Von Kármán crater (186 km in diameter), situated at the center of SPA (Figure 1(b)). The terrain of the landing area is relatively flat, with surface undulations within a range of approximately 60 m. Since the formation of the Von Kármán crater during the pre-Nectarian period, it has undergone complex geological alterations (X. Fu et al. 2020). Initially, before the Imbrian period, the ejecta from the Leibnitz impact reshaped the northern region of the Von Kármán crater. Subsequently, during the Imbrian period, lunar mare basalt flooded the crater floor, including influences from the ejecta of the 82 km Alder impact crater at different periods (J. Huang et al. 2018). These geological activities, including multiple phases of basaltic lava flow, the filling of surrounding impact craters' ejecta, and various impact-related activities, constitute the primary geological features of this region and may obscure paleo-impact craters.

[5] These authors contributed equally.

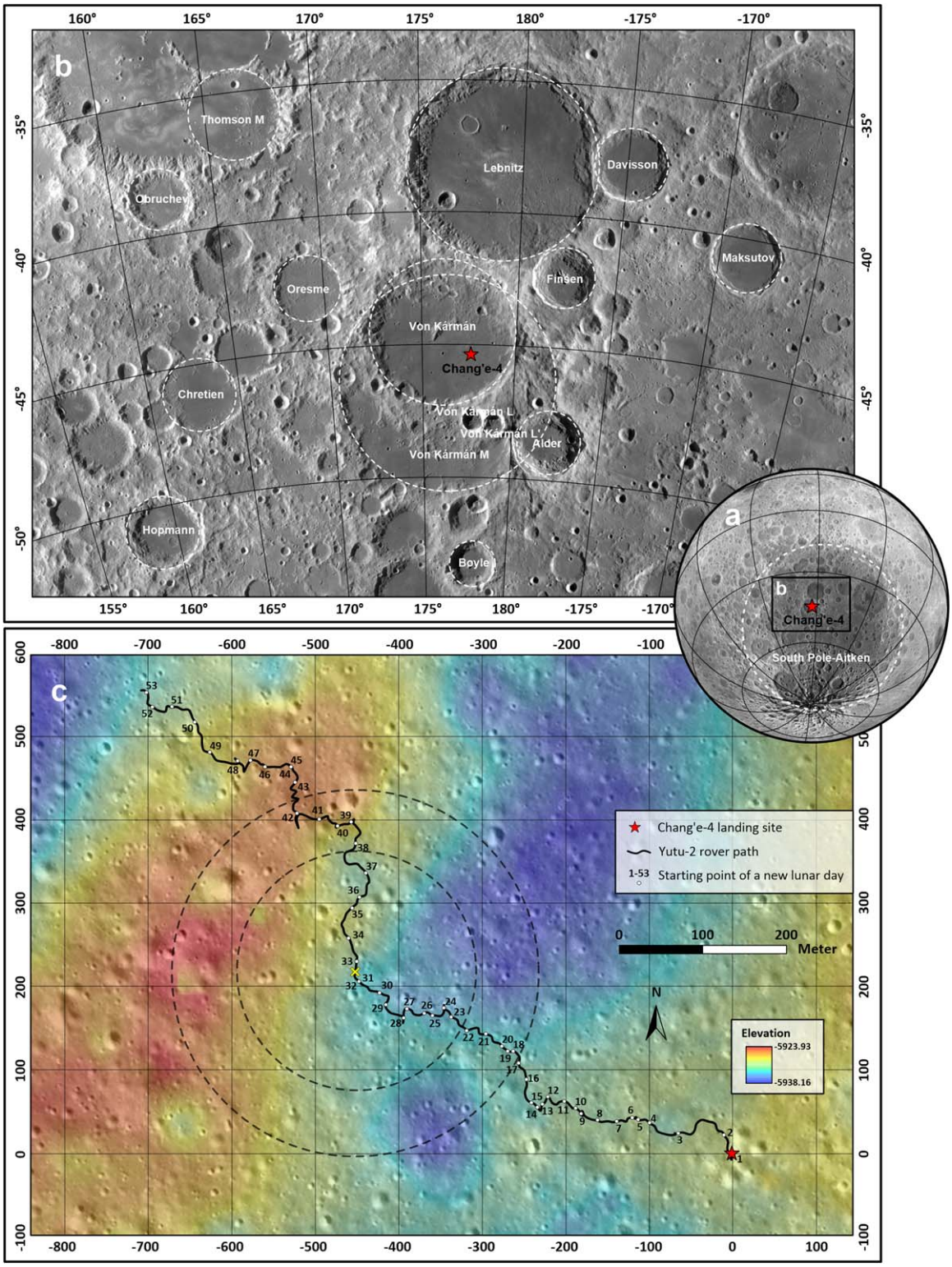

Figure 1. Chang'e-4 landing site and the traversing path of Yutu-2 rover. (a) The location of South Pole–Aitken basin and Chang'e-4 mission landing site on the Moon. (b) Von Kármán crater and vicinity area. The red star represents the Chang'e-4 mission landing site. (c) The path of the Yutu-2 rover during the 53 lunar days. After 53 lunar days of exploration, the Yutu-2 lunar rover has traveled exceeding 1500 m. The yellow cross indicates the potential center of the discovered flat-bottomed paleocrater with a hidden central rebound, with the inner circle represented by a black dashed line denoting the possible crater floor range. The outer circle delineates the potential extent of the entire impact crater with 450 m diameter. (The elevation data: NAC_DTM_CHANGE4; The orthophoto data: NAC_DTM_CHANGE4_M1303619844_140CM).

Initial results from the low-frequency LPR channel reveal the top 400 m subsurface structure near the lunar surface, indicating that the landing site has undergone multiple stages of volcanic activities and the eruption volume decreasing with time (J. Lai et al. 2020; J. Zhang et al. 2020, 2020; Y. Yuan et al. 2021). The high-frequency radar results classify the

shallow subsurface into multiple units, consisting of alternating layers of weathering material, coarse-fine ejecta, and basalt layer (C. Li et al. 2020; C. Ding et al. 2021; Y. Yuan et al. 2021; L. Zhang et al. 2021). In addition, ghost impact craters have been discovered at the Chang'e-4 landing site, buried by lateral ejecta. The bowl shape feature has been identified as a buried crater with a diameter of 150 ± 30 m and a depth of 16 m (L. Zhang et al. 2021; H. Zhou et al. 2022).

With the continuous traverse of the Yutu-2 lunar rover, the newly found lateral structure has provided us with a renewed understanding of this region. In this paper, we discovered a distinctive buried ancient impact crater from an extraterrestrial planet based on the most recent LPR data obtained by Yutu-2. This crater has an undisturbed flat bottom with a hidden central rebound below the crater. Through the analysis of the crater's characteristics and its interaction with subsurface layers, we further propose the formation of the multilayered structure resulting from repeated basaltic lava emplacement.

2. Methods

2.1. Data Processing of LPR Data

The scientific objective of the high-frequency channel is to conduct high-resolution structural imaging within a depth of tens of meters in the Von Kármán crater. To produce an informative radar image, we built on the experience of processing similar data from the Chang'e 3 LPR data, and developed a set of new processing procedures for the CE-4 LPR data:

1. *Data format conversion.* We selected the second channel data collected by antenna B. Chang'e 4 LPR data complies with the standard storage format of the Planetary Data System. We converted the raw data into a binary format for processing, analysis, and imaging.
2. *Ordering of the stitched data*. The data of different lunar days are stored in different multiple files. After reading the data files one by one, they need to be stitched together to form a complete radar profile.
3. *Deletion of duplicate redundant traces.* Yutu-2 rover sometimes stops at specific locations to collect VNIS data. However, the LPR antennas do not stop collecting radar data. It leads to repeated acquisitions in the same place, forming redundant and repeated traces. This step deletes the duplicate traces.
4. *Time lag adjustment.* When the high-frequency LPR channel is operative, the receiving antenna is turned on 28.203 ns earlier than the transmitting antenna. Therefore, this information is redundant and must be deleted.
5. *Removal of the background noise.* The strong reflection off the surface and the lateral noise of the instrument affect the quality of the data. This step removes the horizontal background signals by subtracting the averaging trace.
6. *Bandpass filtering to remove high- and low-frequency noise.* The bandwidth of the high-frequency channel is 250–750 MHz and the bandpass filtering of the same bandwidth was set to remove the signal noise outside this range.
7. *Boosting weaker signals*. Since the signal of the emitted electromagnetic wave becomes weaker from propagation with increasing depth, the energy of the reflected signal also weakens in strength. Consequently, a gain stage is applied as a boost.
8. *Median Filtering*. After gain processing, the entire radar profile (especially in deep locations) still has Gaussian-like noise signals, using median filtering to make the profile clearer.
9. *Channel Equalization*. Due to the deaveraging process used in background removal, it will lead to large differences in amplitude distribution in the lateral direction, and channel equalization makes the amplitude distribution consistent.
10. *Time-depth conversion*. $\varepsilon = 4.5$ is used for time-to-depth conversion.

2.2. Uncertainty of Depth and Thickness

The velocity for time-to-depth conversion is the most important factor in determining the depth of the target and the thickness of the layers, while for radar waves, the wave velocity is calculated from the dielectric constant ε by the following equation,

$$v = \frac{c}{\sqrt{\varepsilon}}.$$

In this paper, $\varepsilon = 4.5$ is used for time-to-depth conversion. Different layers can be detected on the landing site, including regolith, paleoregolith, eject and basalt layer, etc. The permittivity of the Chang'e-4 landing site is considered to fluctuate between 4.5 ± 1.5 by the hyperbolic method as well as other inversion methods (Z. Dong et al. 2020; I. Giannakis et al. 2021; C. Li & J. Zhang 2021). Based on the derived permittivity range, the uncertainty of the converted depth can reach 25%.

For the uncertainty of the thickness of each layer, LPR has a resolution of 0.3 m in vacuum, and ε for time-to-depth conversion also affects the uncertainty. Taking the global $\varepsilon = 4.5$ used for time-to-depth conversion, the thickness of each layer is obtained from top to bottom, respectively, as (I) $10.3^{+4.5}_{-5.6}$, (II) $8.0^{+3.1}_{-3.6}$, (III) $2.4^{+1.2}_{-1.0}$, (IV) $2.7^{+1.0}_{-1.1}$, (V) $3.9^{+2.6}_{-2.2}$, and (VI) $7.5^{+2.8}_{-2.7}$ (Figure 2). The thickness of Layer VII could not be estimated because of the undetectable lower interface.

For a more accurate estimation of layer thickness, varying ε for time-to-depth conversion should be required for different layers. For Layers I and II, as regolith and paleoregolith, the dielectric constant was estimated to be 4.5 by the previous studies, whereas for Layers III, IV, and V, as basaltic layers, the dielectric constants will reach 7.5 ± 2.5 (C. Li et al. 2020). The three estimated layers are further constrained for (III) $1.9^{+0.9}_{-0.8}$, (IV) $2.1^{+0.8}_{-0.9}$, and (V) $3.0^{+2.0}_{-1.7}$.

3. Results

After 53 lunar days of traversing until 2023 March, the Yutu-2 lunar rover has traveled over 1500 m (Figure 1(c)). Simultaneously, the LPR collected radar images along the entire path. Following a series of processing steps (Section 2), we obtained profiles of the high-frequency channel, providing clear imaging of structures within a depth of over 40 m (Figure 2). Focused analyses were conducted at multiple locations (Figure 2(b)) and discussed below:

(1) The surface layer (Layer I), approximately 12 m thick, is generally interpreted to be a regolith layer formed by the weathering of ejecta from the Finsen crater and local materials over an extended period to the current

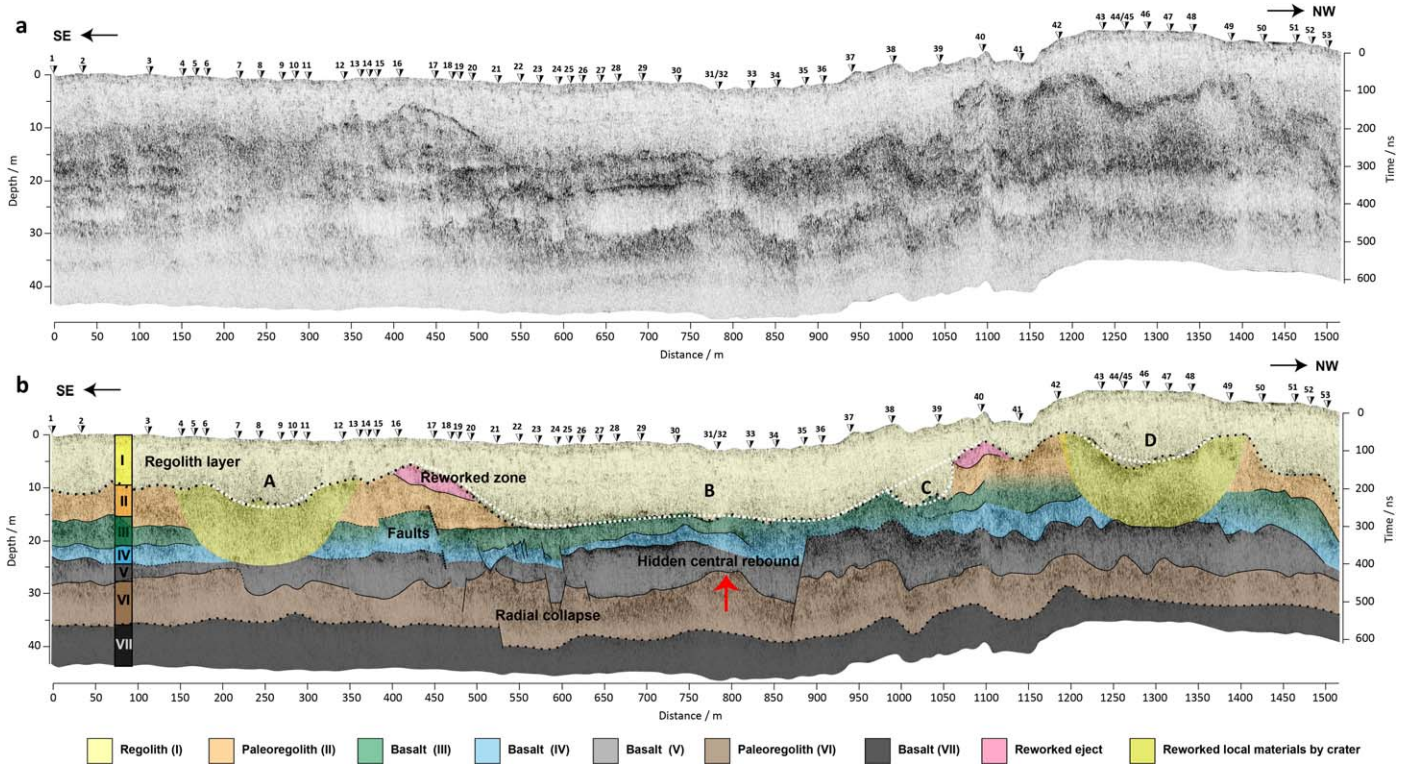

Figure 2. Radar profiles from 53 lunar days with processing details: (a) processed radar image and (b) radar image with interpretations. The surface's shallow yellow area represents the most recent lunar soil layer. Four ancient impact craters are identified within the profile range, including the flat-bottomed paleocrater with a hidden central rebound. The stratigraphic columns illustrate the conditions before the formation of impact craters, comprising: (I) the most recent lunar soil layer, (II) ancient lunar soil, (III)–(V) interbedded basaltic layers or ejecta, (VI) ancient lunar soil, and (VII) basaltic bedrock. $\varepsilon = 4.5$ is used for time-to-depth conversion in both images.

(L. Zhang et al. 2020b; Y. Yuan et al. 2021; H. Cao et al. 2023).

(2) Four identified impact craters (white dashed lines) are observed, labeled A, B, C, and D, with Crater A having been previously identified (L. Zhang et al. 2021). Impact Crater D, similar in morphology to Impact Crater A, is a small, buried crater. Impact Crater B is a larger crater with a central rebound zone, and Crater C may be a small crater hit into the pit wall of Crater B because of asymmetric structures between the right and left sides of Crater B.

(3) The pink areas situated within the rim of Crater B represent the reworked zone probably by ejecta slope slumping. The flat bottom appearance of Crater B is caused by the impact process on the layered structure with dramatically different strengths (W. L. Quaide & V. R. Oberbeck 1968); the central rebound zone below the crater floor is the response of the target to the impact in the stress release stage (H. J. Melosh 1989). The radial collapse (within the red box), and a small fault were generated by postimpact stress changes.

(4) The stratigraphic column (Figure 2(b)) shows seven units: (I) the most recent lunar soil layer, (II) ancient lunar soil, (III)–(V) interbedded basaltic layers or ejecta, (VI) ancient lunar soil, and (VII) basaltic bedrock.

4. Discussion

4.1. The Discovery of a Buried Flat-bottomed Crater on Terrestrial Worlds

Based on the LROC NAC data, LPR data, and Digital Terrain Model (DTM) data, we reconstructed a three-dimensional cross-cutting profile of Crater B (Figure 3(a)). It is hypothesized that this crater was formed by impacting on the ancient loose lunar regolith layer, which was exposed on the surface before the arrival of the ejecta of Finsen crater (J. Lai et al. 2021), overlaying on more rigid basalts. V. R. Oberbeck & W. L. Quaide (1967) conducted a series of experimental impacts on layer-like targets with a weak surface layer ("regolith"). Their experiments indicated that while impacts on a coherent and consistent substrate produce circular bowl-shaped craters, impacts on a substrate covered with fragmented material result in different crater morphologies: as the thickness of the regolith decreases, the shape evolves from bowl-shaped to central mounded, then to flat bottomed, and finally to concentric features. Their laboratory experiments have been confirmed by recent iSALE numerical simulations (N. C. Prieur et al. 2018) and widely observed on other planets (L. E. Senft & S. T. Stewart 2007, 2008). With a well-defined flat floor overlaying on a recessive rebound zone (Figure 2(b)), Crater B could readily be classified as a currently buried paleo flat-bottomed crater. Its morphology indicates the impact reached the interface between the regolith (Layer II) and the substrate (Layer III). The strength of the lower material is much greater than that of the upper material so that it could resist the deformation caused by the impact. Therefore, we hypothesize that the material at the bottom (Layer III of Figure 2(b)) of the crater is a basalt unit and Layer II (Figure 2(b)) is the paleoregolith layer, not a coarse-grained ejecta layer or basalt unit (Y. Yuan et al. 2021; L. Zhang et al. 2021).

On Earth, benefited by high-resolution in situ earthquake data, a complex crater was recently discovered in the Guinea Plateau, West Africa (U. Nicholson et al. 2022): it exhibits an

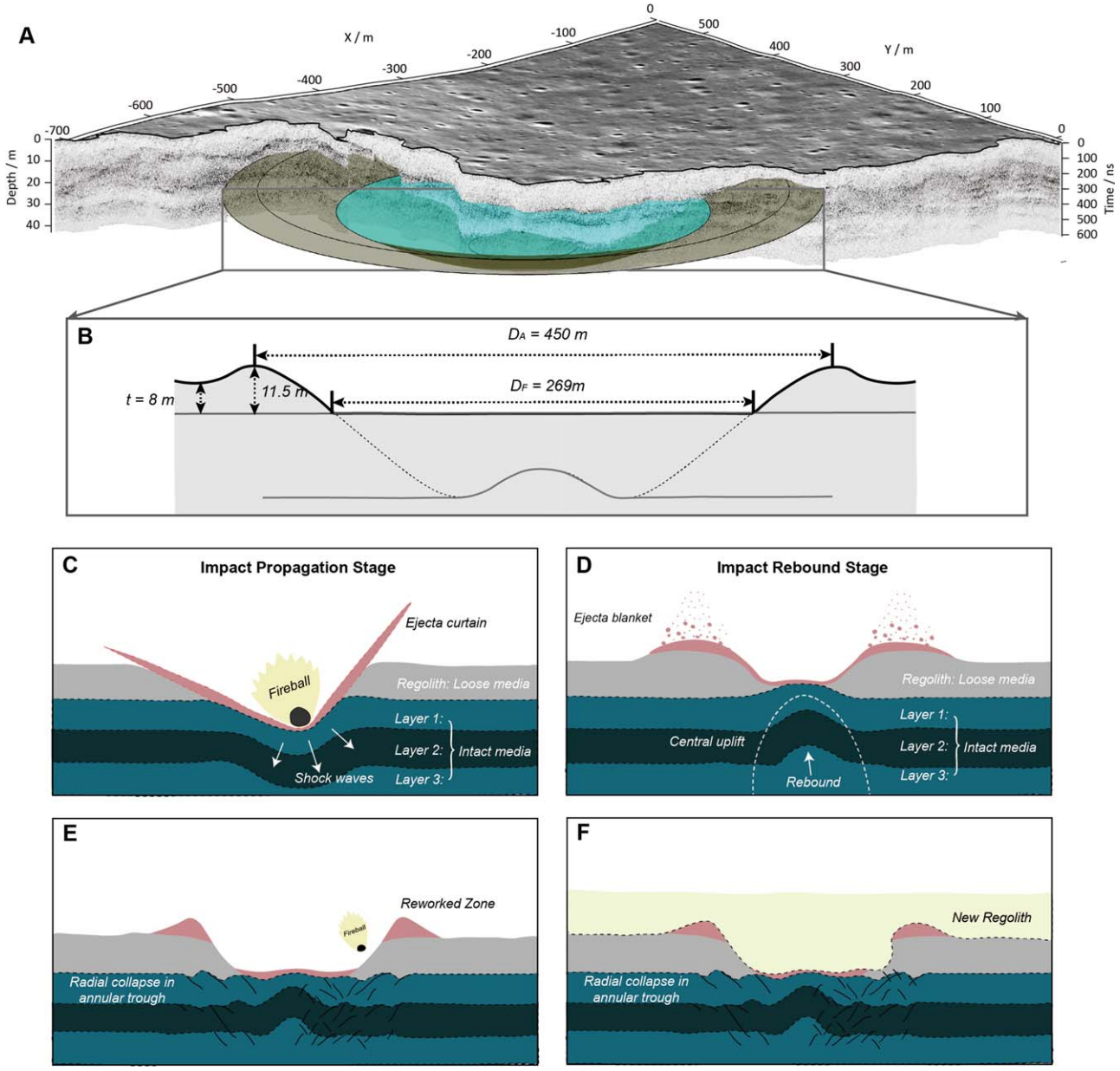

Figure 3. The 3D flat-bottomed paleocrater and its evolutionary model. (a) 3D radar image reveals the 3D flat-bottomed paleocrater. (b) Vertical profile of the flat-bottomed paleocrater with recessive central uplift and parameters. (c)–(f) The evolutionary model of the buried flat-bottomed paleocrater on the Chang'e-4 landing site.

elevated rim above a terraced crater floor, a prominent central peak, and extensive subsurface deformations. Among the 204 identified impact craters on the Earth (Impact Earth Database), this one bears striking similarities to the crater we have identified in the Von Kármán crater. Both of them involve impacts on layered targets with weak-strength surface layers, forming uplifted central peaks (Earth) or recessive central rebound (Moon). They both exhibit radial collapse in an annular trough, fault structures, and a subtle central uplift, eventually buried and covered by subsequent deposits. The difference lies in the fact that the lunar target on the Moon is the weathered paleo lunar regolith, while the Earthly target consists of water layers, which reduces the impact velocity and thus dampens the energy of the impact when it reaches the substrate. In addition, the Earthly impact crater is $\geqslant$8.5 km in diameter, much larger than Crater B, making it become a complex crater. The similarities and differences between these two impact craters shed light on finding more buried craters on all terrestrial planets that may have significant tectonic or environmental consequences.

4.2. The Derivation of Morphological Parameters of Crater B and Its Implications for Its Origin

The flat-bottomed crater, Crater B, can be characterized by three key parameters, i.e., the crater diameter $D_A = 450$ m, the inner ring diameter on the bottom $D_F = 269$ m, and regolith thickness $t = 8$ m (Figure 3(b)). However, the geomorphologic parameters of the studied impact Crater B significantly deviate from the empirical relationship of regolith thickness and D_F/D_A ratios developed by W. L. Quaide & V. R. Oberbeck (1968) experiments (see Figure A1 in the Appendix). D_F/D_A ratio of Crater B is 0.6, which is in the range of 0.2–0.7 but its

D_A/t value far exceeds the theoretical value. The deviation may be due to Crater B being a severely degraded crater. Its slope on the left and right side is 10°.6 and 9°.3, respectively, much smaller than a typical fresh crater (a typical value of 31° for the lunar regolith; W. L. Quaide & V. R. Oberbeck 1968.

Additionally, the diameter of the impact crater simulated by experiments of W. L. Quaide & V. R. Oberbeck (1968) is smaller than 200 m, which is smaller than Crater B and may account for the bias.

Numerical simulations by varying conditions such as target characteristics and impact velocity found that the flat-bottom crater with a similar size to Crater B is more likely to form when the difference of the strength between the two layers of target material is greater than a factor of 200 and the impact velocity is low, e.g., 1 km s^{-1} used for the simulations (N. C. Prieur et al. 2018). Although a primary impact could generate a flat-bottomed crater, the small depth-to-diameter ratio and the low impact speed to preferentially form flat-bottomed craters likely imply Crater B is a secondary crater formed by a low-velocity impact. P. Senthil Kumar et al. (2011; Figure A2 in the Appendix) has found clusters of flat-bottomed craters in the Mare Imbrium with diagnostic secondary patterns, suggesting forming central mound or flat-bottomed craters by secondary cratering is possible. Similar phenomena by clustered impact have been long proven by P. H. Schultz & D. E. Gault (1985).

The secondary craters are generally smaller in size (not more than ∼5% of the primaries), except for the secondaries of large impact basins (P. H. Schultz & J. Singer 1980); hence, the primary crater of Crater B could have a diameter over 8 km. However, it is difficult to constrain primary crater orientation with a single secondary flat-bottomed crater. Based on the geomorphological characteristics of the four flat-bottomed secondary Copernicus craters (P. Senthil Kumar et al. 2011), the slope of the crater wall close to the primary crater is slightly greater than that of the other side (Figure A2 in the Appendix). Crater B is also asymmetric with a relatively large slope on the left side (Figure 2); therefore, the primary crater may be oriented on the eastern, southeastern, or southern side of the Von Kármán crater.

4.3. Stratigraphy and Regolith Growth Rate

Apart from the discovery of the buried flat-bottomed crater with a secondary origin, the LPR data used in this study (Figure 2(a)) also help to reconstruct the stratigraphic column of the landing site and constrain the regolith growth rate of various layers (Layer I, Layer II, and Layer VI; Figure 2(b)). The regolith growth rate not only reflects the impact flux in different periods of lunar history but also the bedrock properties.

For the surface Layer I (0–10 m), it is widely accepted to be a regolith layer forming on the ejecta of the Finsen crater over a long period of space weathering, consisting of fine-grained regolith and coarse-grained ejecta materials (J. Lai et al. 2019; J. Zhang et al. 2020, 2020). The measured thickness of the regolith (Layer I) is about 10 m, thicker than that of the Chang'e-3 (CE-3) and Chang'e-5 (CE-5) landing sites with younger surface age. With the estimated age (2.0–3.5 Ga) of the Finsen crater using the crater counting method (Y. Chang et al. 2021; S. Gou et al. 2021; Y. Lu et al. 2021), the regolith equivalent growth rate of Layer I is calculated as 2.8–5 m Ga^{-1}. The regolith equivalent growth rate at CE-3 and CE-5 landing sites is about 2–4.5 times as high as that at CE-4 landing site (S. Liu et al. 2023; CE-3: 10∼12.5 m Ga^{-1}; CE-5: 11.9 m Ga^{-1}).

For Layers II–V (10–29 m), there are different interpretations of their characteristics. J. Zhang et al. (2020) and Xu et al. (2021) suggested that multilayers are composed of ejecta with different grain sizes or sources. Layers II–IV have also been interpreted as basalt due to the relatively high-frequency shift characteristics (I. Giannakis et al. 2024). The flat-bottomed morphology of Crater B supports the other interpretation: Layers III–V are multilayered basalt flows separated by paleoregolith layers (Y. Yuan et al. 2021; L. Zhang et al. 2021). Layer II is a paleoregolith layer with weaker strength; Layers III–V are multiple basalt flows formed by volcanic events. Radial collapse of the basalt layer due to the impact is observed in radar profiles (Figure 2). Although ejecta and basalts cannot be well distinguished on the basis of their dielectric constants, based on the relationship between the rate of frequency shift and the ilmenite content (A. L. Boivin et al. 2022a, 2022b), the ilmenite contents of different layers can be compared. Layers III–IV may have ilmenite contents higher than 10% with no clear rocks/boulders, indicating they are high-Ti basalts (I. Giannakis et al. 2024), again against their ejecta origin. Considering the strength of the layer, we are more inclined to believe that Layer II is the weathering product of basalt and has retained the high-Ti content of basalt. The thicknesses of Layers III–V are $2.4^{+1.2}_{-1.0}$, $2.7^{+1.0}_{-1.1}$, and $3.9^{+2.6}_{-2.2}$ m, respectively, comparable to the thin basalt layers in the lunar nearside revealed by the NAC images, suggesting lava eruption intensity of the Von Kármán crater is similar to the lunar nearside.

The average thickness of the paleoregolith Layer II is about 8 m. It was formed on the underlying bedrock basalts (Layer III) before the coverage of Finsen ejecta for a period of 0.1–0.5 Ga, considering the surface age of basalts is 2.2–2.5 Ga (J. Haruyama et al. 2009; J. H. Pasckert et al. 2018; Y. Yuan et al. 2021) or 3.2∼3.6 Ga (J. Huang et al. 2018; Y. Lu et al. 2021) and the Finsen crater age is 2.0 Ga (Y. Chang et al. 2021) or 3.1–3.5 Ga (S. Gou et al. 2021; Y. Lu et al. 2021). In addition, we observed that the slope of Crater B is around 10°.6 corresponding to a degradation age of ∼1 Ga (A. T. Basilevskii 1976) (Figure A3 in the Appendix). It suggests the exposure age of Layer III is no larger than 1.0 Ga to form Layer II regolith (C. Ding et al. 2021; Y. Lu et al. 2021; Y. Yuan et al. 2021); therefore, the regolith growth age for Layer II is further constrained to be 0.5–1.0 Ga, corresponding to a production rate of 8–16 m Ga^{-1}. This value is obviously higher than Layer I, indicating the regolith growth is relatively faster before the Finsen impact. The formation speed is mainly affected by the impact flux; however, during the time period between 2.0 and 3.0 Ga, the impactor flux is nearly a constant after the exponential decay from 3.5 to 3.0 according to the Neukum chronology function (G. Neukum et al. 2001). The exotic materials (ejecta) could contribute to the thickness of the regolith. In addition, J. W. Head & L. Wilson (2020) mentioned that "autoregolith" formed by late-stage gas-rich magma can increase the thickness of the regolith layer. Such late volcano structure, e.g., ring-moat dome structure has been found in the Von Kármán crater (F. Zhang et al. 2017).

Note that the depths of Layers VI–VII are close to the penetration limit of LPR, leading to the uncertainties of their geologic interpretations. For Layer VII at a depth of about

36 m, no obvious reflections are detected from the deepest signals. Combined with crater geomorphologic analysis, previous studies interpreted it as the basalt bedrock (X.-H. Fu et al. 2020; J. Huang et al. 2018; Y. Yuan et al. 2021; L. Zhang et al. 2021). Layer VI overlying Layer VII might be another paleoregolith layer on top of the basalt due to its relatively strong scattering properties. Layer VI is the deepest paleo regolith layer detected by this study, with a thickness ranging from 4.8 to 10.3 m (7.5 m on average). However, its growth rate is not easy to obtain without the age of the underlying ancient basalts. According to J. H. Pasckert et al. (2018), the majority of mare eruption on the lunar farside occurred between 3.0 and 3.8 Ga; therefore, Layer VII basalts most likely onset between 3.5 and 3.8 Ga (older than Layers III–V with an age of 3.5 Ga; J. Huang et al. 2018), close to the peak of lunar farside volcanism. In such a high-intensity phase, its lava flow thickness (>10 m) is larger than later erupted Layers III–V basalts around 2.5–4 m.

5. Conclusion

This study presents findings from the high-frequency LPR data obtained by the Chang'e-4 mission, revealing a buried flat-bottomed paleocrater located about 15 m beneath the Von Kármán crater. Our reconstruction of the crater (450 m in diameter and 11.5 m in depth) suggests that it is likely a secondary impact structure formed by a low-velocity impact on a layered target (basalt and the overlying regolith), which subsequently underwent modification and compression. The primary crater is potentially located to the east, southeast, or south of the Von Kármán crater. Evidence of central rebound and radial collapse further supports this interpretation.

We reconstruct the stratigraphic column of the lunar landing site, revealing the regolith growth rates of various layers. Layer I (0–10 m) is identified as a regolith formed from Finsen crater ejecta, with a growth rate of 2.8–5 m Ga^{-1}, indicating extensive space weathering. Layers II–V (10–29 m) are interpreted with Layer II as a paleoregolith and Layers III–V as basalt flows, suggesting a complex volcanic history for that period. The average thickness of Layer II is about 8 m, with a growth rate of 8–16 m Ga^{-1}, indicating faster regolith formation prior to the Finsen impact. Exotic materials (ejecta) may have contributed to the thickness of the regolith. Additionally, "autoregolith" formed by late-stage gas-rich magma can also increase the thickness of the regolith (J. W. Head & L. Wilson 2020). Due to the influence of the signal-to-noise ratio, the characteristics of Layers VI–VII remain uncertain. Layer VII may represent older basalt bedrock from 3.5 to 3.8 Ga, while Layer VI, averaging 7.5 m in thickness and exhibiting strong scattering properties, is likely another paleoregolith layer overlying the basalt.

We determined the source of subsurface materials primarily based on the morphology of impact craters. The findings underscore the effectiveness of LPR technology in investigating subsurface lunar structures, offering essential data for reconstructing the Moon's geological history and advancing our understanding of lunar evolution. These insights also hold significant implications for impact processes on other planetary bodies.

Acknowledgments

All the authors appreciate the Chang'e-4 team for making a great successful mission and providing scientific data. The Chang'e-4 LPR data can be accessed by visiting the LUNAR AND PLANETARY DATA RELEASE SYSTEM website (https://moon.bao.ac.cn). The images and elevation data of the landing area can be obtained from the website (https://wms.lroc.asu.edu/lroc). This work was supported by the Science and Technology Development Fund of Macau (FDCT) (grant No. 0014/2022/A1), the Science and Technology Development Fund of Macau (FDCT) (grant No.0021/2024/RIA1), the Science and Technology Development Fund of Macau (FDCT) (grant No.0158/2024/AFJ), the Science and Technology Development Fund of Macau (FDCT) (grant No.002/2024/SKL), the National Natural Science Foundation of China (grant No. 42104141), the National Natural Science Foundation of China (grant Nos. 12103020 and 12363009), and Natural Science Foundation of Jiangxi Province (grant No. 20224BAB211011).

Appendix
Supplementary Materials

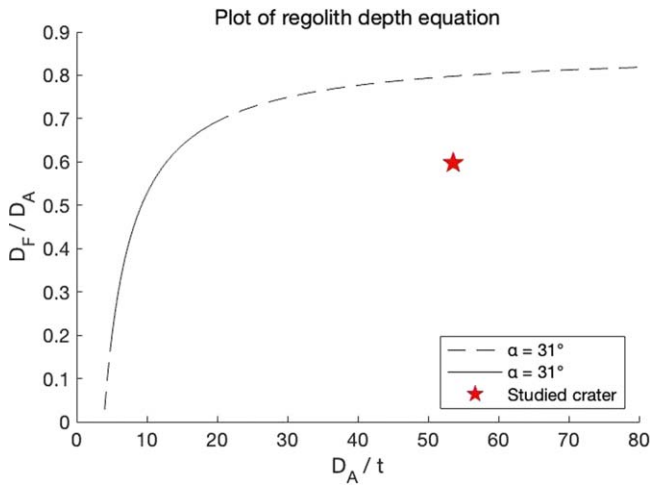

Figure A1. Plot of the regolith depth equation (W. L. Quaide & V. R. Oberbeck 1968). The solid line indicates the region where regolith depth measurements are most useful. The dashed line indicates regions where either the diameter ratio (D_F/D_A) is nearly constant (upper dashed line) or where the normalized regolith depth (D_A/t) is nearly constant (lower dashed line), therefore providing little meaningful regolith depth data. The red pentagram is the impact crater studied.

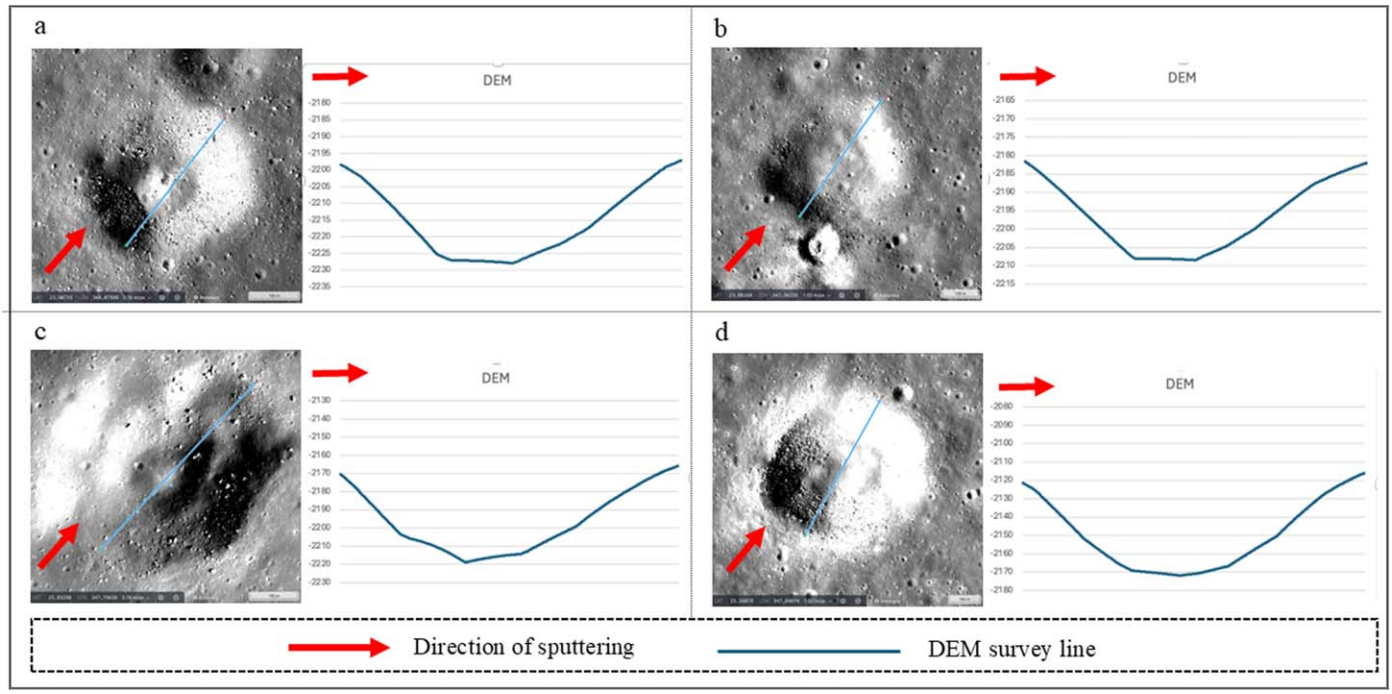

Figure A2. Elevation information for the four secondary flat-bottomed impact craters from Copernicus crater (G. Neukum et al. 2001). (A), (B), (C), and (D): the image maps of the four secondary flat-bottomed impact craters and the elevation tables of their corresponding survey lines. Red arrows show the direction of sputtering of material from the primary crater; topography data is from SLDEM2015 + LOLA (M. K. Barker et al. 2016).

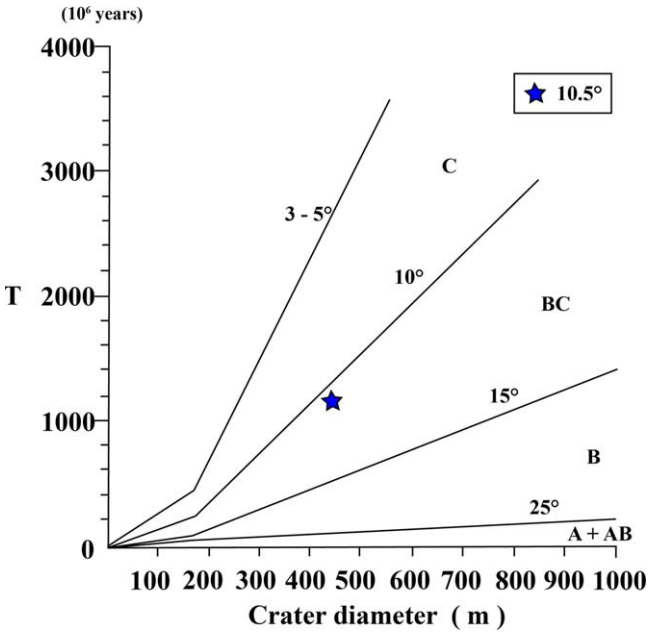

Figure A3. Impact crater degradation age model (A. T. Basilevskii 1976). (A), (B), and (C) are used to distinguish the degree of degradation of the impact crater from fresh to old. The blue pentagram is the impact crater studied.

ORCID iDs

Yuqi Qian https://orcid.org/0000-0001-7119-5501
Yi Xu https://orcid.org/0000-0001-8894-525X
Jialong Lai https://orcid.org/0000-0002-2157-2767

References

Barker, M. K., Mazarico, E., Neumann, G. A., et al. 2016, Icar, 273, 346
Bart, G. D., Nickerson, R. D., Lawder, M. T., & Melosh, H. J. 2011, Icar, 215, 485
Basilevskii, A. T. 1976, LPSC, 1, 1005
Boivin, A. L., Tsai, C-A., Hickson, D. C., Ghent, R. R., & Daly, M. G. 2022a, JGRE, 127, e2022JE007199
Boivin, A. L., Tsai, C-A., Hickson, D. C., Ghent, R. R., & Daly, M. G. 2022b, JGRE, 127, e2022JE007200
Cao, H., Xu, Y., Xu, L., et al. 2023, GeoRL, 50, e2022GL101413
Chang, Y., Xiao, Z., Wang, Y., et al. 2021, E&PP, 5, eepp2021007
Ding, C., Xiao, Z., Wu, B., et al. 2021, JGRE, 126, e2021JE006917
Dong, Z., Fang, G., Zhao, D., et al. 2020, GeoRL, 47, e2020GL089264
Evans, A. J., Soderblom, J. M., Andrews-Hanna, J. C., Solomon, S. C., & Zuber, M. T. 2016, GeoRL, 43, 2445
Fu, X., Qiao, L., Zhang, J., Ling, Z., & Li, B. 2020, RAA, 20, 008
Giannakis, I., Martin-Torres, J., Su, Y., et al. 2024, Icar, 408, 115837
Giannakis, I., Zhou, F., Warren, C., & Giannopoulos, A. 2021, GeoRL, 48, e2021GL092866
Gou, S., Yue, Z., Di, K., et al. 2021, Icar, 360, 114370
Haruyama, J., Ohtake, M., Matsunaga, T., et al. 2009, Sci, 323, 905
Head, J. W., & Wilson, L. 2020, GeoRL, 47, e2020GL088334
Huang, J., Xiao, Z., Flahaut, J., et al. 2018, JGRE, 123, 1684
Lai, J., Xu, Y., Bugiolacchi, R., et al. 2020, NatCo, 11, 3426
Lai, J., Xu, Y., Bugiolacchi, R., et al. 2021, GeoRL, 48, e2021GL095133
Lai, J., Xu, Y., Zhang, X., et al. 2019, GeoRL, 46, 12783
Li, C., Liu, D., Liu, B., et al. 2019, Natur, 569, 378
Li, C., Su, Y., Pettinelli, E., et al. 2020, SciA, 6, eaay6898
Li, C., & Zhang, J. 2021, RemS, 13, 1387
Liu, S., Santos, L. A., Ning, S., et al. 2023, JGRE, 128, e2022JE007675
Lu, Y., Wu, Y., Michael, G. G., et al. 2021, Icar, 354, 114086
Melosh, H. J. 1989, Impact cratering: a geologic process (Oxford: Clarendon Press)
Neukum, G., Ivanov, B. A., & Hartmann, W. K. 2001, in Chronology and Evolution of Mars, ed. R. Kallenbach, J. Geiss, & W. K. Hartmann (Dordrecht: Springer), 55
Nicholson, U., Bray, V. J., Gulick, S. P. S., & Aduomahor, B. 2022, SciA, 8, eabn3096
Oberbeck, V. R., & Quaide, W. L. 1967, JGR, 72, 4697
Osinski, G. R., Melosh, H. J., Andrews-Hanna, J., et al. 2023, RvMG, 89, 339
Pasckert, J. H., Hiesinger, H., & Van Der Bogert, C. H. 2018, Icar, 299, 538
Prieur, N. C., Rolf, T., Wünnemann, K., & Werner, S. C. 2018, JGRE, 123, 1555
Qian, Y., Xiao, L., Head, J. W., et al. 2021, GeoRL, 48, e2021GL095341
Quaide, W. L., & Oberbeck, V. R. 1968, JGR, 73, 5247
Schultz, P. H., & Gault, D. E. 1985, JGRB, 90, 3701
Schultz, P. H., & Singer, J. 1980, LPSC, 3, 2243

Senft, L. E., & Stewart, S. T. 2007, JGRE, 112, E11002
Senft, L. E., & Stewart, S. T. 2008, M&PS, 43, 1993
Senthil Kumar, P., Senthil Kumar, A., Keerthi, V., et al. 2011, P&SS, 59, 870
Stickle, A. M., & Schultz, P. H. 2013, M&PS, 48, 1638
Wilcox, B. B., Robinson, M. S., Thomas, P. C., & Hawke, B. R. 2005, M&PS, 40, 695
Wu, W., Li, C., Zuo, W., et al. 2019, NatGe, 12, 222
Xu, L., Zhang, X., Qiao, L., & Lai, J. 2021, AJ, 162, 29
Yuan, Y., Zhu, P., Xiao, L., et al. 2021, E&PSL, 569, 117062
Zhang, F., Head, J. W., Basilevsky, A. T., et al. 2017, GeoRL, 44, 9216
Zhang, J., Zhou, B., Lin, Y., et al. 2020, NatAs, 5, 25
Zhang, L., Li, J., Zeng, Z., et al. 2020, GeoRL, 47, e2020GL088680
Zhang, L., Xu, Y., Bugiolacchi, R., et al. 2021, E&PSL, 564, 116912
Zhou, H., Feng, X., Ding, C., et al. 2022, ITGRS, 60, 1